Title
Ultrafast X-ray scattering offers a structural view of excited-state charge transfer

Journal
Proceedings of the National Academy of Sciences of the United States of America, 118(19)

ISSN
0027-8424

Authors
Yong, Haiwang
Xu, Xuan
Ruddock, Jennifer M
et al.

Publication Date
2021-05-11

DOI
10.1073/pnas.2021714118

Peer reviewed

Ultrafast X-ray scattering offers a structural view of excited-state charge transfer

Haiwang Yong[a], Xuan Xu[a], Jennifer M. Ruddock[a], Brian Stankus[b], Andrés Moreno Carrascosa[a], Nikola Zotev[c,d], Darren Bellshaw[c,d], Wenpeng Du[a], Nathan Goff[a], Yu Chang[a], Sébastien Boutet[e], Sergio Carbajo[e], Jason E. Koglin[e], Mengning Liang[e], Joseph S. Robinson[e], Adam Kirrander[c,d,1], Michael P. Minitti[e], and Peter M. Weber[a,1]

[a]Department of Chemistry, Brown University, Providence, RI 02912; [b]Department of Chemistry and Biochemistry, Western Connecticut State University, Danbury, CT 06810; [c]EaStCHEM, School of Chemistry, University of Edinburgh, Edinburgh EH9 3FJ, United Kingdom; [d]Center for Science at Extreme Conditions, University of Edinburgh, Edinburgh EH9 3FJ, United Kingdom; and [e]Linac Coherent Light Source, Stanford Linear Accelerator Center National Accelerator Laboratory, Menlo Park, CA 94025

Edited by Shaul Mukamel, University of California, Irvine, CA, and approved March 16, 2021 (received for review October 16, 2020)

Intramolecular charge transfer and the associated changes in molecular structure in N,N′-dimethylpiperazine are tracked using femtosecond gas-phase X-ray scattering. The molecules are optically excited to the 3p state at 200 nm. Following rapid relaxation to the 3s state, distinct charge-localized and charge-delocalized species related by charge transfer are observed. The experiment determines the molecular structure of the two species, with the redistribution of electron density accounted for by a scattering correction factor. The initially dominant charge-localized state has a weakened carbon–carbon bond and reorients one methyl group compared with the ground state. Subsequent charge transfer to the charge-delocalized state elongates the carbon–carbon bond further, creating an extended 1.634 Å bond, and also reorients the second methyl group. At the same time, the bond lengths between the nitrogen and the ring-carbon atoms contract from an average of 1.505 to 1.465 Å. The experiment determines the overall charge transfer time constant for approaching the equilibrium between charge-localized and charge-delocalized species to 3.0 ps.

ultrafast dynamics | femtosecond | X-ray scattering | charge transfer | excited state

Understanding the dynamic process of photoinduced charge transfer is expected to lead to many practical applications, including efficient photovoltaic systems, the development of photocatalysts, and better materials for energy storage (1–3). Charge transfer redistributes the electrons in a molecule and is typically associated with changes in the molecular geometry (2). On the fastest time scale, electrons move so rapidly that the nuclei appear frozen, a phenomenon known as charge migration (4–10). When time scales approach the typical vibrational motions of molecules, that is, tens of femtoseconds (10^{-14} s), the nuclei can adjust their positions, often resulting in localization of electronic charge and permanent changes in molecular geometry (11). While exhibiting a rich phenomenology on different time scales, it is evident that electron charge transfer and nuclear dynamics are intrinsically coupled (12–17). An accurate determination of the changes in molecular structure during charge transfer is therefore of great interest from both applied and fundamental perspectives.

New scientific technologies, in particular X-ray free-electron lasers (XFEL) (18, 19) and MeV ultrafast electron diffraction (20), have made it possible to study structural dynamics in the ultrafast regime. Recent femtosecond gas-phase scattering experiments have successfully tracked structural changes during chemical reactions (21–26) and probed specific signatures of excited electronic states (27, 28). Given the emerging ability of ultrafast gas-phase scattering to record both nuclear and electronic structure (25, 27, 28), we use time-resolved gas-phase X-ray scattering to study the photoinduced intramolecular charge transfer in an organic molecule, N,N′-dimethylpiperazine (DMP, $C_6H_{14}N_2$), shown in Fig. 1. In its ground electronic state, DMP has C_{2h} symmetry with two equivalent ionization centers, one on each nitrogen atom. Valence ionization, or in the present case excitation to an electronic Rydberg state (29), induces charge transfer between the two nitrogen atoms, making DMP a prototype for exploring electron lone-pair interactions and charge transfer (30–32).

Previously, energy relaxation pathways and charge transfer in electronically excited DMP were explored using Rydberg fingerprint spectroscopy (33), a form of photoelectron spectroscopy. As depicted in Scheme 1, the investigations by Deb et al. (33) found that optical excitation at 207 nm prepares the molecule in a 3p Rydberg state, creating a state with a localized charge in the molecular core (3pL). Internal conversion to 3s then leads to charge-localized (3sL) and charge-delocalized (3sD) conformers with 230 and 480 fs time constants, respectively. The charge transfer proceeds as the molecules explore the 3s potential energy surface. An equilibrium between 3sL and 3sD structures is eventually established with an overall time constant of 2.65 ps, with the forward and backward first-order kinetic time constants for the transformation 3.4 and 12.0 ps, respectively (33).

A limitation in the prior spectroscopic work is that the photoelectron peaks are assigned by comparing measured binding energies with computational results and that the molecular structures that underlie the calculations cannot not be independently

Significance

Charge transfer plays a fundamental role in many areas of chemistry, physics, biology, and materials science. The spatial redistribution of electrons is typically associated with changes in the molecular geometry. A comprehensive understanding of this process requires atomic spatial resolution and femtosecond temporal resolution. Here, we exploit an X-ray free-electron laser to determine the excited-state structures during charge transfer with sub-Ångström resolution. Important behaviors such as bond elongation and contraction and reorientation of functional groups during the charge transfer are discovered, demonstrating the substantial information on excited-state molecular structure that becomes accessible through ultrafast X-ray scattering measurements.

Author contributions: A.K., M.P.M., and P.M.W. designed research; H.Y., X.X., J.M.R., B.S., W.D., N.G., Y.C., S.B., S.C., J.E.K., M.L., J.S.R., M.P.M., and P.M.W. performed research; H.Y., X.X., J.M.R., B.S., A.M.C., N.Z., D.B., W.D., N.G., and Y.C. analyzed data; and H.Y., A.K., and P.M.W. wrote the paper.

The authors declare no competing interest.

This article is a PNAS Direct Submission.

[1]To whom correspondence may be addressed. Email: adam.kirrander@ed.ac.uk or peter_weber@brown.edu.

This article contains supporting information online at www.pnas.org/lookup/suppl/doi:10.1073/pnas.2021714118/-/DCSupplemental.

Published May 4, 2021.

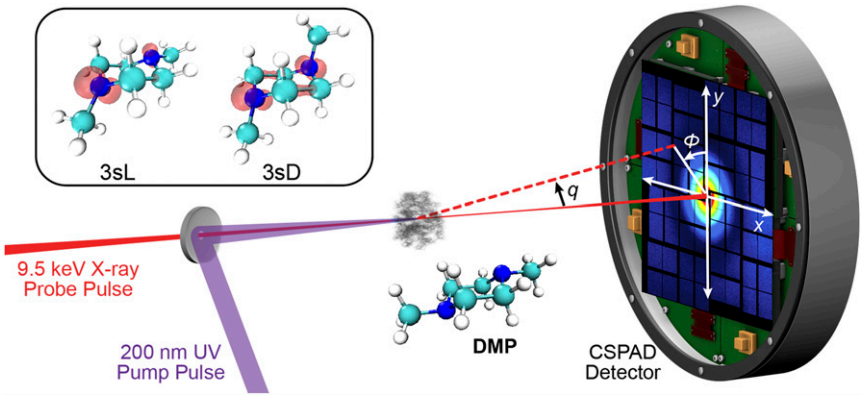

Fig. 1. A schematic illustration of the experimental setup. The ground-state molecules (DMP) were excited by 200 nm ultraviolet pump pulses, and the transient structures were probed by 9.5 keV X-ray pulses at variable time delays. The scattering signals were recorded on a CSPAD detector. The inset shows the calculated spin density, which gives the difference in density of electrons with spin up and spin down, of the charge-localized DMP (3sL) and charge-delocalized DMP (3sD) in the 3s Rydberg states at isovalues of 0.1 electron/Å^3.

determined in the experiments. This is compounded by the fact that theoretical calculation of charge-localized and charge-delocalized excited states is challenging. Widely used computational methods sometimes give unsatisfactory results (34), and even results from high-level computations can be controversial (35–37). This has led to interesting discussions about whether a stable charge-localized structure exists in the DMP cation at all and about the validity of different exchange functionals within density functional theory to study the charge localization in DMP molecules (34). Considering the general experimental and theoretical interest in this system, direct structural measurements would be invaluable. The current study uses ultrafast time-resolved X-ray scattering to observe the structural relaxation dynamics in DMP. This provides a wealth of information, making it possible to test key assumptions of the photoelectron study. Most importantly, we determine the molecular structures of the charge-localized and -delocalized excited states.

Results

The time-resolved X-ray scattering experiment is illustrated in Fig. 1. A 200 nm optical pump laser excites room temperature, gaseous DMP to the transient excited states. X-rays with 9.5 keV mean energy are generated at the Linac Coherent Light Source (LCLS) and scatter from the optically excited molecules. The optical laser and the X-rays propagate collinearly, with their linear polarizations perpendicular to each other. Single-shot scattering patterns are detected on a 2.3 megapixel Cornell-SLAC pixel array detector (CSPAD) (38) and binned according to the delay time between the pump laser and X-ray probe pulses. The time-dependent signals are expressed as percent differences (21, 39):

$$\%\Delta I(q,\phi,t) = 100\frac{I_{\text{on}}(q,\phi,t) - I_{\text{off}}(q,\phi)}{I_{\text{off}}(q,\phi)}, \qquad [1]$$

where ϕ is the azimuthal angle on the detector, q the magnitude of the momentum transfer vector, $I_{\text{on}}(q,\phi,t)$ the optical pump laser-on signal at delay time t, and $I_{\text{off}}(q,\phi)$ the laser-off reference signal. By using percent difference signals, poorly defined experimental parameters, for example pixel noise, background signals, and gas pressure fluctuations, largely cancel out. The percent difference signal depends on the fraction of molecules that are optically excited, a scalar quantity that is determined during the experimental analysis. During the experiment, we keep the optical excitation laser intensity low to minimize multiphoton processes (40–42).

The first stage in the analysis is to decompose the two-dimensional, percent difference pump-probe scattering images into isotropic and anisotropic components using the following equation (43):

$$\Delta I(\phi,q,t) = \frac{1}{2}\left(3\left(\cos(\phi)\sqrt{1-\left(\frac{\lambda q}{4\pi}\right)^2}\right)^2 - 1\right)\Delta I_{\text{aniso}}(q,t) + \Delta I_{\text{iso}}(q,t), \qquad [2]$$

where ϕ is the azimuthal angle on the detector, q the magnitude of the momentum transfer vector, as before, and λ is the X-ray wavelength. The isotropic rotationally averaged percent difference signal $\Delta I_{\text{iso}}(q,t)$ contains all the intrinsic information in the molecular frame, while additional information about the transition dipole moment (TDM) and the rotational alignment of the molecule in the laboratory frame are given by the anisotropic component (43), $\Delta I_{\text{aniso}}(q,t)$.

We use the anisotropic signal to determine the orientation of the TDM of the initially excited 3p state in the molecular frame (43). The optical pump laser preferentially excites molecules with the TDM oriented parallel to the linear polarization of the optical pump pulse in the laboratory frame, giving rise to a marked anisotropy in the experimental percent difference scattering image recorded at 10 fs delay time shown in Fig. 2. Comparison of theoretical and experimental patterns show that the TDM vector cannot be aligned with the C_2 symmetry axis (the z-axis shown in Fig. 2) of the molecule, as this would yield scattering images with the opposite orientation. This is consistent with the general fact that the TDM cannot be perpendicular to a mirror plane. To experimentally determine the orientation of the TDM, theoretical scattering images are calculated for TDM directions from 0 to

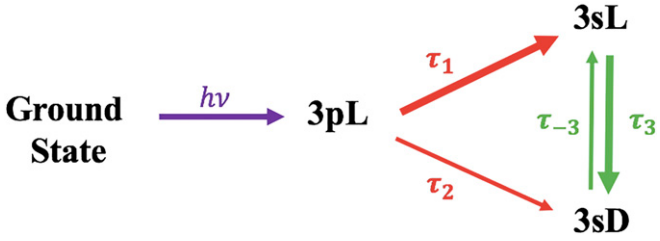

Scheme 1. Reaction pathway for Rydberg-excited DMP as determined previously (33).

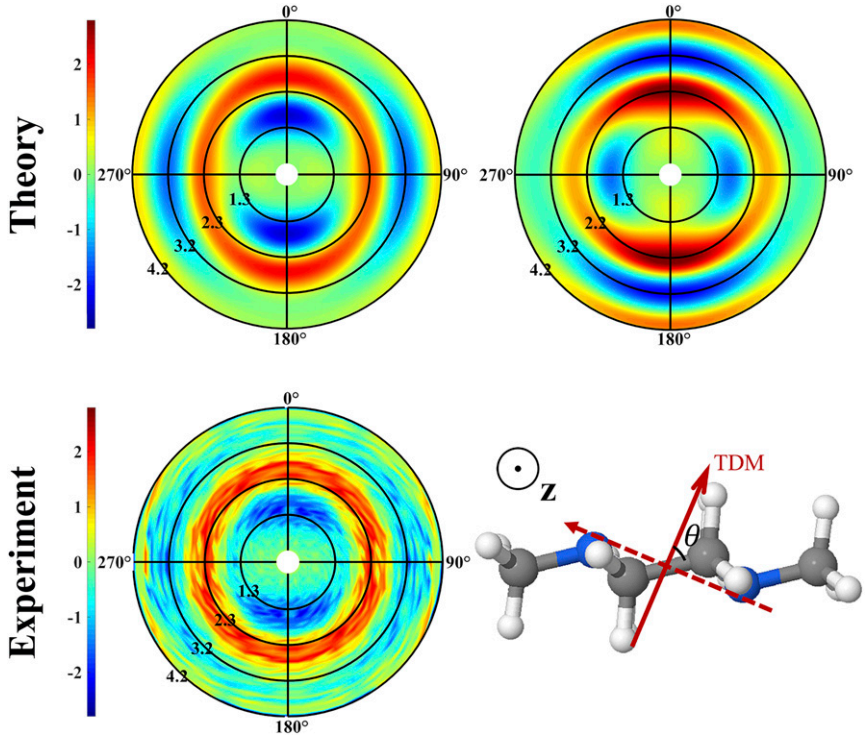

Fig. 2. The anisotropic pump-probe scattering patterns. (*Top*) Computed patterns for TDM parallel (top left, direction of red solid arrow indicated in *Bottom Right*) and perpendicular (top right, direction of red dashed arrow indicated in *Bottom Right*) to the optimal TDM direction in the σ_h plane. (*Bottom*, *Left*) Experimental pattern at 10 fs. (*Bottom*, *Right*) Direction of TDM illustrated in the mirror plane, with the *z*-axis aligned with the C_2 symmetry axis of the ground-state DMP molecule.

180 degrees in the σ_h symmetry molecular plane and compared with the experimentally observed pattern. The best-fit theoretical pattern is shown in Fig. 2, *Top Left*, and is found to have a TDM direction with an angle θ of $53^{\circ} \pm 3^{\circ}$ to the direction of central C–C bond (the direction of the red solid arrow in Fig. 2). For contrast, the theoretical scattering pattern corresponding to a TDM orientation perpendicular to the optimal TDM direction is also included in Fig. 2 (*Top Right*, with the direction indicated by a red dashed arrow).

We now focus the analysis on the time-dependent isotropic percent difference signal, shown in Fig. 3, to unveil the kinetics and structural dynamics of DMP following laser excitation. We adopt the same overall reaction scheme to model the kinetics as the previous photoelectron study (33) shown in Scheme 1, which leads to charge-localized (3sL) and charge-delocalized (3sD) conformers, although our analysis makes no assumption regarding the nature of these conformers. An equilibrium is attained from the combination of forward (τ_3) and backward (τ_{-3}) reactions. Fitting the time dependence of the experimental data with this reaction model and taking the scattering signals of the individual conformers as adjustable parameters, results in an excellent fit as shown in Fig. 4 and *SI Appendix*, Fig. S2. The fit equation is as follows (44):

$$\Delta I_{iso}(q,t) = \gamma\left(\sum_{\alpha} S_{\alpha}(q)F_{\alpha}(t)\right) * g(t), \qquad [3]$$

where $S_\alpha(q)$ is the fitted isotropic scattering pattern of transient structure α, while $F_\alpha(t)$ is the corresponding time-dependent population as determined by the kinetic scheme. The scalar γ represents the excitation probability, and $g(t)$ is a Gaussian function that characterizes the instrument response. The kinetic parameters extracted from this fit, shown in Table 1, are in reasonable agreement with the spectroscopic values obtained in the previous study, even though the excitation wavelengths are slightly different (200 nm in the current and 207 nm in the previous study). The differences in the kinetic parameters are mostly within the respective error bars in both experiments, with other small discrepancies possibly arising from the difference in excitation wavelengths. The X-ray scattering results indicate a charge transfer process

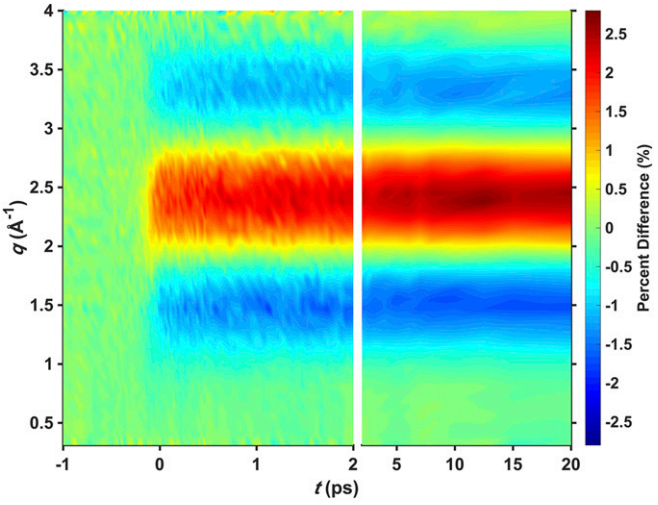

Fig. 3. The isotropic component, $\Delta I_{iso}(q,t)$ (see Eq. **2**), of the experimental percent difference scattering signal as a function of delay time t (ps) and the magnitude of the momentum transfer vector q (Å^{-1}), with the value of the percent difference indicated by the color bar. Note the change of scale in the time axis at 2 ps.

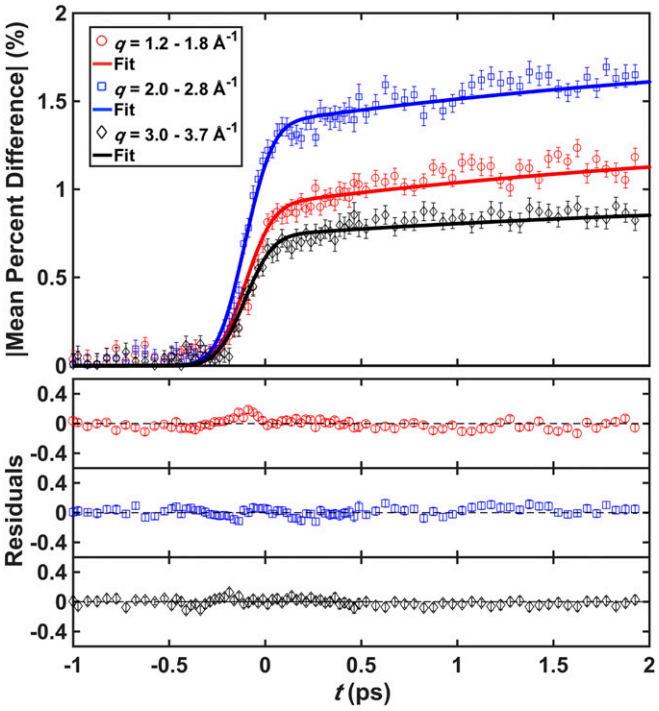

Fig. 4. Absolute values of the percent difference isotropic scattering signals $\Delta I_{iso}(q,t)$ averaged over three different q ranges. Shown are the experimental data (red circles, blue squares, and black diamonds) with 1σ uncertainties and the kinetic fits (solid lines). The lower panel shows the residuals; that is, the difference between the experimental values and the fit.

with a time constant of 3.6 ps for charge delocalization and a time constant of 19.0 ps for charge relocalization, making for an overall approach of the equilibrium with a $\left(\tau_3^{-1} + \tau_{-3}^{-1}\right)^{-1} = 3.0$ ps time constant. This is in excellent agreement with the previously determined 2.65 ps time constant from photoelectron spectra by Deb et al. (33) (reference *SI Appendix*, *Supplementary Note* 1 for details of the kinetic fits). One should note that Table 1 designates the forward reaction as the charge-delocalization process and the backward reaction as the charge relocalization. A further evaluation of this assignment is discussed later in this article.

The kinetic fits described above yield the q-dependent scattering signals of the two individual reaction products. These are shown in Fig. 5. The difference patterns correspond to the difference between the ground-state and the excited-state transient species (see Eqs. **4** and **5** in *Methods*). Since the ground-state structure is well known, the percent difference patterns reflect the deviation of the excited-state molecular structures from the ground state. Each of the species in Scheme 1 differs from the ground-state molecule in their molecular geometry and in their electron density distribution, and the differences lead to changes in the scattering corresponding to the net change in electron density. The changes in molecular geometry often dominate the percent difference scattering signal, but accounting for the redistribution of the electron density due to specific electronic states is important for the retrieval of correct molecular structures (25, 27).

A key assumption in the previous photoelectron studies (33) is the assignment of observed binding energy peaks to the localized and delocalized molecular forms. In order to test this assumption, our analysis ignores, but only in an initial analysis, the change in electron density distributions upon optical excitation. In this initial treatment, the molecular scattering patterns are calculated using the independent atom model (IAM) (45). Two million structures are created from a Wigner distribution (46, 47) using calculated vibrational normal modes for the charge-localized and charge-delocalized molecules, respectively, (see *Methods* for details) and their IAM scattering patterns are compared with the experimentally determined patterns in Fig. 5. These structures sample a large conformational space that is confined to energetically allowed conformations that could potentially be accessed by the molecule in 3sL and 3sD states. By comparing each experimentally derived pattern with IAM patterns computed from these sampled structures, the least-squares fitting errors of all theoretical patterns from the pool were obtained for each of two experimental curves in Fig. 5. These errors are then plotted against each structural parameter such as the interatomic distances and the bond angles. In general, the least-squares error varies as a function of any given structural parameter in a normal-like distribution (25, 47). The peak centers of these distributions were thus taken to represent the best-fitting structural parameters. This procedure works for any pool of structures that is sufficiently expansive and dense to contain structures in the vicinity of the correct structure (47), and the choice of the Wigner distribution is a matter of convenience.

The analysis reveals unambiguously that the photoelectron spectroscopy assignment is correct: the scattering pattern with the smaller modulation depth (black circles in Fig. 5) is associated with an asymmetric 3sL structure where one of the amine groups is nearly planar while the other remains sp^3 hybridized, and the larger amplitude pattern (blue diamonds in Fig. 5) is from the symmetric 3sD structure where both amine groups are nearly planar (see full results in *SI Appendix*, *Supplementary Note* 2). The pump-probe X-ray experiment is therefore able to determine the identity of the species in Scheme 1 without reference to electronic structure calculations.

Having confirmed the assignment of the scattering patterns in Fig. 5, we proceeded to further refine the molecular structures. In this second step, we account for the change in electron density for the charge-localized and -delocalized states as shown in Fig. 6 compared with the electronic ground state. Since this effect is solely due to the electron density redistribution in the excited electronic state, we refer to it as the electronic contribution (see Eq. **5** in *Methods*) to the overall percent difference scattering pattern (27). The calculations, which include elastic and inelastic scattering contributions, are described in detail in the *Methods* section. From Fig. 6, we notice that the electronic structure changes contribute at most a −2% percent difference, which is dwarfed by the total change which spans −20% to 30% for the delocalized 3sD signal shown in Fig. 5. Nevertheless, at $q \approx 1$ Å^{-1}, where the electronic contributions are significant, they constitute almost a quarter of the overall −8% difference. The electronic contributions therefore cannot be neglected. This is consistent with the recent finding that in order to determine the structure of excited molecules correctly, the changes in electron density must be accounted for when analyzing the X-ray scattering data (25, 27). As shown previously, the electronic contribution for excited states with Rydberg character depends weakly on the molecular geometry and can be approximated by a constant correction term (25). In the present case, we find that the electronic contributions for 3sL and 3sD are sufficiently different that they must be

Table 1. Time constants with 1σ uncertainties according to Scheme 1 obtained in a global fit of all time-dependent X-ray scattering data and the comparable values from previous photoelectron spectra

	X-ray scattering (this work)	Spectroscopic results (33)
τ_1 (fs)	80 ± 40	230 ± 30
τ_2 (fs)	630 ± 190	480 ± 70
τ_3 (ps)	3.6 ± 0.3	3.4 ± 0.1
τ_{-3} (ps)	19.0 ± 2.7	12.0 ± 0.8

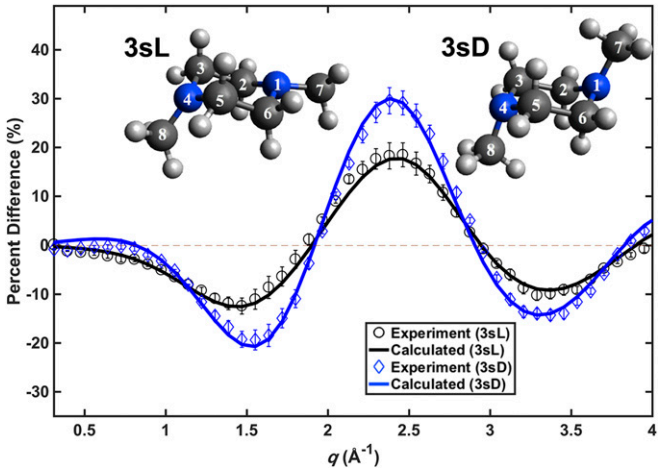

Fig. 5. Experimental and calculated percent difference isotropic scattering patterns and molecular structures of DMP in the charge-localized 3sL and the charge-delocalized 3sD conformers. The experimental results (circles and diamonds) are extracted from the kinetics fit with 3σ uncertainties and divided by the excitation fraction γ, determined from the fit. Calculated scattering patterns (solid lines) are for the experimentally determined optimal structural parameters with electronic contributions included. (*Inset*) Representative geometries of 3sL and 3sD.

included in the treatment explicitly. Inspecting the Rydberg orbitals of 3sL and 3sD in Fig. 6, we propose that the reason for this is that the positive charge in the core region redistributes to both nitrogen atoms during charge delocalization, with an associated adjustment of the Rydberg orbital. This is consistent with the calculated spin density as illustrated in the Fig. 1 insert. The charge is localized dominantly on the planar nitrogen in 3sL while equally distributed amongst the two nitrogen atoms in 3sD. Furthermore, there is some net spin density in the molecular core distributed through the carbon–carbon bonds, further indicating a delocalized character in 3sD.

Based on these considerations, we add the 3sL electronic correction to the localized geometry structures in the structure pool and likewise the 3sD correction to the delocalized structures. Using the IAM for the geometrical structure, we recalculate corrected theoretical scattering patterns for all two million structures contained in the pool. The structural analysis is then repeated with the improved theoretical patterns, resulting in excellent agreement between the calculated scattering patterns (black and blue solid lines in Fig. 5) and the experimental signals. The small discrepancy for the charge-localized curves around 2.2 Å^{-1} could originate from the broadening of the nuclear distributions in the 3sL state reported by Deb et al. (33). This analysis yields the excitation fraction with 1σ uncertainty according to Eq. **3** as $\gamma = 9.4 \pm 0.3\%$. This is sufficiently low to suggest that multiphoton excitation or ionization processes are not likely to adversely affect our results (reference *SI Appendix*, *Supplementary Note* 1 for more discussion).

The analysis above yields precise excited-state structures that are largely derived from experimental observations. The structures can therefore serve as experimental benchmarks for further excited-state structure calculations. The structural parameters for all bond lengths and two characteristic nonbonded interatomic distances in 3sL and 3sD are shown in Fig. 7. Representative three-dimensional molecular renderings corresponding to these parameters, obtained as the best fit to the 28 nonhydrogenic interatomic distances, are shown in Fig. 5 with the Cartesian coordinates given in *SI Appendix*, Table S3.

To put the structural parameters of the Rydberg-excited molecules into context, Fig. 7 compares them with optimized structures of the charge-localized cation and the charge-delocalized cation calculated from high-level complete active space self-consistent field theory (CASSCF) as reported by Gałyńska et al. (37). Although the ion structures are not necessarily identical to the structures in the 3s Rydberg state, they are likely rather similar (25, 34). Indeed, Fig. 7 shows good agreement. Our analysis for extracting the excited-state structures does not intrinsically constrain the molecular symmetry. Even so, atom–atom distances related by symmetry are found to be equal within the stated uncertainties, further supporting the validity of the experiment and the analysis method.

Analyzing the changes in geometry and examining the results in Fig. 7 and *SI Appendix*, Table S1 and the structures in Fig. 5, it is apparent that the most significant difference between the localized and the delocalized excited-state structures relates to the position of the methyl groups. In the ground electronic state, the amine groups are sp^3 hybridized, but the excitation of an electron from the lone-pair orbital of the nitrogen atom to the diffuse Rydberg orbital changes it to favor sp^2 hybridization. Indeed, the N_1 atom with the localized charge assumes a torsional angle of 165° (averaged over two equivalent angles), whereas N_4 remains at 93°. This causes a shortened C_7 to C_8 distance of 5.311 Å compared with 5.649 Å for ground-state structure. Once the charge delocalizes, the two nitrogen atoms share one charge, causing them to assume equal torsional angles of 89° (averaged over four equivalent angles) and to shorten the C_7 to C_8 distance to 5.200 Å. The computational results for the molecular ion are quite similar, even though the exact angles are slightly different. Since the N–C bonds for the two nitrogen atoms in the localized structure are not equivalent, their measurement uncertainty is larger than in the delocalized structure (see first two rows of Fig. 7).

Both the experimental results for Rydberg excitation and the computational results for the ion suggest that the central C–C bond weakens upon excitation. While the bond length is 1.530 Å in the ground electronic state, it stretches to 1.571 Å in the charge-localized species (averaged over two equivalent bonds). This is in almost perfect agreement with the ion calculation, which gives 1.574 Å. The charge transfer to the delocalized state weakens this bond even further to 1.634 Å, a very long distance for a C–C bond. This leads to an elongation of the N_1 to N_4 distance from 2.888 Å in the ground electronic state to 2.904 Å in charge-localized 3s

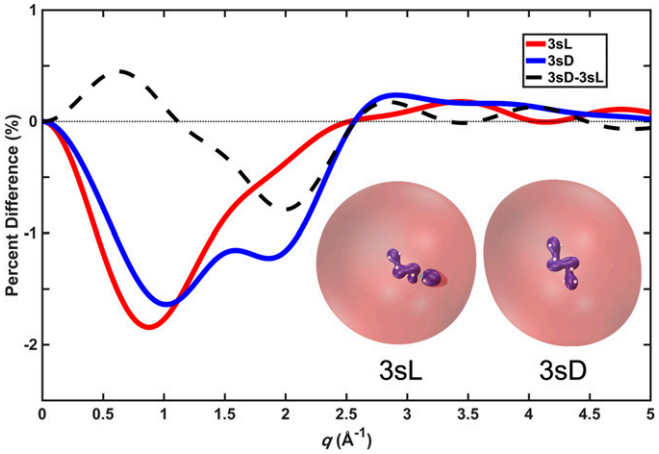

Fig. 6. Calculated percent difference scattering patterns caused by electronic structure changes, assuming 100% excitation. The 3sL (red solid line) and 3sD (blue solid line) curves are the electronic contribution difference between the charge-localized structure in the 3s and electronic ground states and between the charge-delocalized structure in the 3s and electronic ground states, respectively. The black dashed line shows the difference between the 3sD and 3sL curves. The inset shows calculated 3sL and 3sD Rydberg orbitals, respectively, rendered at 0.0005 Å$^{-3/2}$ isovalues.

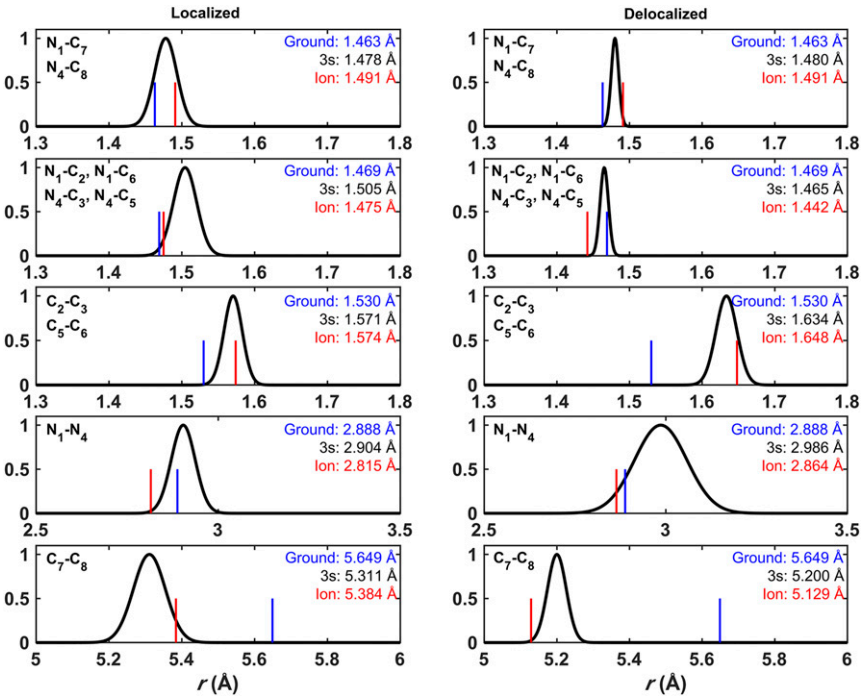

Fig. 7. Experimentally determined structural parameters for the Rydberg-excited charge-localized (left column) and charge-delocalized (right column) species, compared with computed values for the molecular ion and the molecular ground state. The black curve is the Gaussian function $e^{-\frac{1}{2}\left(\frac{x-\mu}{\sigma}\right)^2}$. Here, μ is the experimentally determined interatomic distance in the 3s electronic state, averaged over symmetry-equivalent distances as listed in the left legend of each panel, and σ is the error as listed in *SI Appendix*, Table S1 (propagated when there are several symmetry-equivalent distances). The red lines are distances calculated at the DMRG-CASSCF(19,20)/aug-cc-pVDZ level of theory for the ionic localized and ionic delocalized ground states (37). The blue lines are the ground-state structure distances calculated from CCSD/aug-cc-pVDZ reported by Cheng et al. (34). (Full interatomic distances and characteristic angles are given in *SI Appendix*, Table S1.)

state and a further elongation to 2.986 Å in the charge-delocalized 3s state as shown in Fig. 7. Conversely, the distances between the nitrogen atoms and the ring-carbon atoms contract during the charge transfer from an average of 1.505 to 1.465 Å (averaged over four bonds), that is, by 0.040 Å. This is again in excellent agreement with the ion calculations, where the bond contraction upon delocalization is 0.033 Å. These findings prove the effect of charge delocalization on the molecular structure and the importance of structural dynamics in the full characterization of charge transfer processes.

Discussion

The advent of XFELs with their outstanding brightness and ultrashort pulse durations heralds a new age of molecular structure determination. It is now possible to experimentally determine the structure of short-lived optically excited states with a precision that approaches traditional ground-state measurements. Accurate interpretation of experimental scattering patterns requires corrections to account for the changes in electron density distributions upon excitation. These corrections are obtained from electronic structure calculations. As the computational input appears as a correction term, the X-ray structures are largely experimentally determined. Direct inversion of a scattering pattern from an isotropic gas-phase sample is not possible. We thus determine molecular structures by comparing simulated scattering patterns from a pool of structures with experimentally measured signals. With the upcoming improvements in XFEL technology (48) and the ongoing development of robust methods for scattering data analysis (49, 50), we anticipate that both electronic and nuclear structural dynamics during chemical reactions will be directly determined from X-ray scattering experiments, providing a comprehensive view of the coupled electron and nuclear motions in chemical dynamics. Moreover, it is possible to extract scattering patterns corresponding to transient species because the time-dependent scattering signals are comprised of orthogonal contributions (51), with the time dependence following the kinetic process and the q dependence arising from the patterns of the individual transient species.

We have applied this methodology to the photoinduced charge transfer of DMP, revealing kinetic time scales that are in close agreement with previous photoelectron spectroscopy results. Importantly, we are able to determine the orientation of the TDM in the molecular frame, determine the full molecular structures of the charge-localized and charge-delocalized species, and confirm the redistribution of charge. We find that the delocalization of charge with a time constant of 3.6 ps is associated with a weakening of the C–C bond by 0.063 to 1.634 Å. The most significant difference between the localized and the delocalized excited-state structures relates to the position of the methyl groups. These experimentally determined excited-state structures provide valuable benchmarks for the ongoing refinement of the computational chemistry methods and bring insight into the detailed dynamics of charge transfer in polyatomic molecules.

Methods

Experimental Details. The time-resolved gas-phase X-ray scattering setup has been introduced previously (40, 52). The optical pump laser uses the fourth harmonic of a 120 Hz Ti:Sapphire laser operating at 800 nm, generating pulses at 200 nm with ∼80 fs pulse duration and ∼1 μJ/pulse energy on target. The gaseous DMP sample pressure at the interaction region is ∼5 Torr, controlled by a piezoelectric needle valve. Both pump pulse energy and gas pressure are optimized to reduce background signal and achieve less than 10% excitation probability. The X-ray probe pulses contain $\sim 10^{12}$ photons/pulse at 9.5 keV photon energy, with ∼30 fs pulse duration and 120 Hz repetition rate. The pump and probe pulses are focused collinearly into the scattering cell, with approximate spot sizes (full width at half maximum) of 30 μm for the X-rays and

50 μm for the laser. The interaction length is kept small at 2.4 mm to prevent excessive absorption attenuation of the ultraviolet beam at the downstream end of the interaction region. The gas cell and the detector were in vacuum, with an average background pressure outside the scattering cell of 1.4×10^{-4} Torr, mostly comprised of DMP that flowed out of the windowless scattering cell (40). The time delay between the pump and probe pulses is controlled by an electronic delay stage, with the timing jitter monitored by a spectrally encoded cross correlator achieving a 30 fs time resolution (53). In order to achieve the desired noise level (<0.1%), the X-ray intensity of each shot is measured by a photodiode downstream of the scattering cell. A 2.3 megapixel CSPAD is used to detect shot-to-shot scattered X-rays. Details of the detector distance calibration, the error analysis of the measured scattering signals, and the decomposition into isotropic and anisotropic signals have been discussed previously (40, 54).

Structural Analysis. The concept of the structure determination method for extracting experimentally determined structural parameters from time-resolved X-ray scattering patterns has been discussed in detail previously. (47) A pool of molecular structures that is sufficiently large to likely contain the sought molecular structure is essential. Because the nuclear geometry of DMP-L^+ and DMP-D^+ are relatively close to the structures of 3sL and 3sD, we sample a large pool of possible structures by displacing their geometries starting from the DMP-L^+ and DMP-D^+ structures. Specifically, to sample the structural pools of 3sL and 3sD properly, we calculated the vibrational normal modes of DMP at the ion minimum-energy localized structure and delocalized structure, respectively, using ab initio electronic structure calculations at the UMP2/aug-cc-pVDZ level of theory in the Molpro software (55). An ensemble of one million geometries is sampled from a quantum Wigner distribution at 1,000 K using SHARC software (56) based on the calculated vibrational normal modes of DMP-L^+ to represent a large range of charge-localized structural space that could potentially be accessed by the molecule in the 3sL state. We use a relatively large scaling temperature (1,000 K) to make sure the displaced geometries are expansive enough to include the target structures (47). Similarly, another ensemble of one million geometries was sampled for the 3sD state. Considering that the C–H bond lengths are well known and do not vary much, and that X-ray signals are not very sensitive toward the positions of hydrogen atoms (57), we fix the C–H bond lengths of all sampled geometries at 1.09 Å to reduce the number of molecular degrees of freedom in the structural analysis. To obtain representative structures corresponding to the best-fit structural parameters, the structures in the pool that gave the smallest fit errors across the 28 non-hydrogenic interatomic distances were chosen to represent the 3sL and 3sD geometries, with their ball-stick structures shown in the Fig. 5 inset of the main text. The complete set of coordinates is given in *SI Appendix*, Table S3. The absolute differences between the interatomic distances calculated from the representative structures and corresponding best-fit structural parameters are given as uncertainties in *SI Appendix*, Table S1, reflecting the uncertainty due to the discrete sampling of the structural space. A comprehensive investigation of various uncertainties when using the structural analysis method was reported in a previous publication (47).

Calculation of Electronic Excited States. Prior studies have shown that self-interaction–corrected density functional theory (SIC-DFT) is well suited for the calculations of Rydberg-excited states (58), including charge-localized and charge-delocalized 3s states of DMP (34). To obtain accurate excited-state electron densities for the electronic scattering pattern corrections, we performed excited-state calculations for the 3sL and 3sD states using the SIC-DFT method. Since the potential energy surfaces of Rydberg states generally track the potential energy surfaces of the ionic states (25, 34), the structures of the charge-localized cation and the charge-delocalized cation optimized using the density matrix renormalization group (DMRG)-CASSCF(19,20)/aug-cc-pVDZ level of theory were adopted as 3sL and 3sD structures during the SIC-DFT calculations (37). The selected structural parameters for these structures are also included as theoretical results in Fig. 7 and *SI Appendix*, Table S1 for comparison with experimentally determined Rydberg structures.

The SIC-DFT calculations were carried out using the grid-based implementation of the projector augmented wave method (GPAW) program (59) with a uniform, real space grid representation of the wavefunctions. The Rydberg state calculations were carried out with SIC-DFT using the local-density approximation (LDA) functional (60) and a cubic cell with 25 Å sides and 0.15 Å grid spacing. To calculate the electron densities and the binding energies, the Rydberg orbitals were first obtained using SIC-DFT for the ground state. The total energy of the Rydberg-excited state was calculated using SIC-DFT and the Delta Self-Consistent Field method (61) where one electron was removed from the highest occupied molecular orbital and placed in the desired Rydberg orbital. The all-electron densities of 3sL and 3sD state were then extracted using the get_all_electron_density class implemented in GPAW. The binding energy of the Rydberg state was calculated by subtracting the total energy of the Rydberg-excited state from that of the ion. The SIC-DFT–calculated binding energies are given in *SI Appendix*, Table S2 and are in excellent agreement with previous experimental values measured by photoelectron spectroscopy (34). The spin densities and Rydberg orbitals calculated using SIC-DFT are shown in the inset of Figs. 1 and 6 of the main text, respectively.

Decomposition of the Percent Difference Scattering Signal. The theoretical percent difference scattering signal, assuming 100% excitation, is calculated by the following equation (27):

$$\Delta S_{\text{theory}}(q,\mathbf{R}') = 100\frac{I_{\text{exc}}(q,\mathbf{R}') - I_{\text{X}}(q,\mathbf{R}_0)}{I_{\text{X}}(q,\mathbf{R}_0)}, \quad [4]$$

where $I_{\text{exc}}(q,\mathbf{R})$ is the excited-state scattering intensity and $I_{\text{X}}(q,\mathbf{R})$ the ground-state scattering, with q the momentum transfer amplitude and $\mathbf{R}$ the molecular geometry. In Eq. **4**, $\mathbf{R}'$ represents the nuclear geometry of the molecule in the excited state at pump-probe delay t and $\mathbf{R}_0$ the ground-state equilibrium structure before laser excitation. It has been shown previously that it is conceptually useful to insert a null contribution, $0 = I_{\text{X}}(q,\mathbf{R}') - I_{\text{X}}(q,\mathbf{R}')$, in order to rewrite Eq. **4** as follows (27):

$$\Delta S_{\text{theory}}(q,\mathbf{R}') = 100\frac{I_{\text{exc}}(q,\mathbf{R}') - I_{\text{X}}(q,\mathbf{R}')}{I_{\text{X}}(q,\mathbf{R}_0)} + 100\frac{I_{\text{X}}(q,\mathbf{R}') - I_{\text{X}}(q,\mathbf{R}_0)}{I_{\text{X}}(q,\mathbf{R}_0)}, \quad [5]$$

where the first term is the electronic contribution reflecting the difference in scattering from the excited and ground electronic states at a given geometry $\mathbf{R}'$, while the second term is the nuclear contribution indicating solely the difference in scattering from changes in the molecular geometry. The rotationally averaged elastic scattering intensities are obtained numerically from the calculated electron density $\rho(\boldsymbol{r})$ based on the Waller–Hartree theory (50). Here, $\rho(\boldsymbol{r})$ is a three-dimensional array extracted directly from the get_all_electron_density class implemented in GPAW as described in the previous section. The inelastic contribution to scattering is approximated by tabulated atomic form factors (45). To calculate the electronic contributions for 3sL and 3sD as shown in Fig. 6 of the main text, we calculate the scattering patterns $I_{3s}(q,\mathbf{R}_{3sL})$, $I_{3s}(q,\mathbf{R}_{3sD})$, $I_{\text{X}}(q,\mathbf{R}_{3sL})$, $I_{\text{X}}(q,\mathbf{R}_{3sD})$, and $I_{\text{X}}(q,\mathbf{R}_0)$ from the electron densities generated by GPAW and use the first term in Eq. **5**. In order to ensure an accurate ground-state scattering pattern as a reference, we adopt the ground-state DMP structure optimized using high-level ab initio calculation [coupled cluster with single and double excitations (CCSD)/aug-cc-pVDZ] reported in ref. 34.

Data Availability. All study data are included in the article and *SI Appendix*.

ACKNOWLEDGMENTS. This research was supported by the US Department of Energy, Office of Science, Basic Energy Sciences under Award DE-SC0017995. H.Y. was supported, in part, by the NSF (Grant CHE-1953839). The work was further supported by Engineering and Physical Sciences Research Council (EPSRC) Grant EP/V006819/1 and Leverhulme Trust Grant RPG-2020-208 (to A.K.), a Carnegie Trust PhD Scholarship (to N.Z.), and an EPSRC PhD Studentship from the University of Edinburgh (to D.B.). Use of the LCLS, SLAC National Accelerator Laboratory, is supported by the US Department of Energy, Office of Science, Office of Basic Energy Sciences under Contract No. DE-AC02-76SF00515.

1. A. H. Zewail, Femtochemistry: Atomic-scale dynamics of the chemical bond using ultrafast lasers (Nobel lecture). *Angew. Chem. Int. Ed. Engl.* **39**, 2586–2631 (2000).
2. H. J. Wörner *et al*., Charge migration and charge transfer in molecular systems. *Struct. Dyn.* **4**, 061508 (2017).
3. P. D. Frischmann, K. Mahata, F. Würthner, Powering the future of molecular artificial photosynthesis with light-harvesting metallosupramolecular dye assemblies. *Chem. Soc. Rev.* **42**, 1847–1870 (2013).
4. A. I. Kuleff, L. S. Cederbaum, Charge migration in different conformers of glycine: The role of nuclear geometry. *Chem. Phys.* **338**, 320–328 (2007).
5. S. Lünnemann, A. I. Kuleff, L. S. Cederbaum, Charge migration following ionization in systems with chromophore-donor and amine-acceptor sites. *J. Chem. Phys.* **129**, 104305 (2008).
6. S. R. Leone *et al*., What will it take to observe processes in 'real time'? *Nat. Photonics* **8**, 162–166 (2014).

7. F. Lépine, M. Y. Ivanov, M. J. J. Vrakking, Attosecond molecular dynamics: Fact or fiction? *Nat. Photonics* **8**, 195–204 (2014).
8. F. Calegari *et al*., Ultrafast electron dynamics in phenylalanine initiated by attosecond pulses. *Science* **346**, 336–339 (2014).
9. P. M. Kraus *et al*., Measurement and laser control of attosecond charge migration in ionized iodoacetylene. *Science* **350**, 790–795 (2015).
10. D. Cho, J. R. Rouxel, M. Kowalewski, J. Y. Lee, S. Mukamel, Attosecond x-ray diffraction triggered by core or valence ionization of a dipeptide. *J. Chem. Theory Comput.* **14**, 329–338 (2018).
11. M. Vacher, M. J. Bearpark, M. A. Robb, J. P. Malhado, Electron dynamics upon ionization of polyatomic molecules: Coupling to quantum nuclear motion and decoherence. *Phys. Rev. Lett.* **118**, 083001 (2017).
12. M. D. Newton, Quantum chemical probes of electron-transfer kinetics–The nature of donor-acceptor interactions. *Chem. Rev.* **91**, 767–792 (1991).
13. C. C. Moser, J. M. Keske, K. Warncke, R. S. Farid, P. L. Dutton, Nature of biological electron transfer. *Nature* **355**, 796–802 (1992).
14. N. Ge *et al*., Femtosecond dynamics of electron localization at interfaces. *Science* **279**, 202–205 (1998).
15. A. T. Yeh, C. V. Shank, J. K. McCusker, Ultrafast electron localization dynamics following photo-induced charge transfer. *Science* **289**, 935–938 (2000).
16. S. M. Falke *et al*., Coherent ultrafast charge transfer in an organic photovoltaic blend. *Science* **344**, 1001–1005 (2014).
17. E. Najafi, T. D. Scarborough, J. Tang, A. Zewail, Fourdimensional imaging of carrier interface dynamics in p-n junctions. *Science* **347**, 164–167 (2015).
18. P. Emma *et al*., First lasing and operation of an angstrom-wavelength free-electron laser. *Nat. Photonics* **4**, 641–647 (2010).
19. W. Decking *et al*., A MHz-repetition-rate hard X-ray free-electron laser driven by a superconducting linear accelerator. *Nat. Photonics* **14**, 391–397 (2020).
20. S. P. Weathersby *et al*., Mega-electron-volt ultrafast electron diffraction at SLAC National accelerator laboratory. *Rev. Sci. Instrum.* **86**, 073702 (2015).
21. M. P. Minitti *et al*., Imaging molecular motion: Femtosecond X-ray scattering of an electrocyclic chemical reaction. *Phys. Rev. Lett.* **114**, 255501 (2015).
22. J. Yang *et al*., Imaging CF_3I conical intersection and photodissociation dynamics with ultrafast electron diffraction. *Science* **361**, 64–67 (2018).
23. T. J. A. Wolf *et al*., The photochemical ring-opening of 1,3-cyclohexadiene imaged by ultrafast electron diffraction. *Nat. Chem.* **11**, 504–509 (2019).
24. M. R. Ware, J. M. Glownia, N. Al-Sayyad, J. T. O'Neal, P. H. Bucksbaum, Characterizing dissociative motion in time-resolved x-ray scattering from gas-phase diatomic molecules. *Phys. Rev. A (Coll. Park)* **100**, 033413 (2019).
25. B. Stankus *et al*., Ultrafast X-ray scattering reveals vibrational coherence following Rydberg excitation. *Nat. Chem.* **11**, 716–721 (2019).
26. T. Kierspel *et al*., X-ray diffractive imaging of controlled gas-phase molecules: Toward imaging of dynamics in the molecular frame. *J. Chem. Phys.* **152**, 084307 (2020).
27. H. Yong *et al*., Observation of the molecular response to light upon photoexcitation. *Nat. Commun.* **11**, 2157 (2020).
28. J. Yang *et al*., Simultaneous observation of nuclear and electronic dynamics by ultrafast electron diffraction. *Science* **368**, 885–889 (2020).
29. R. S. Mulliken, Rydberg states and rydbergization. *Acc. Chem. Res.* **9**, 7–12 (1976).
30. R. Hoffmann, Interaction of orbitals through space and through bonds. *Acc. Chem. Res.* **4**, 1–9 (1971).
31. A. M. Brouwer, F. W. Langkilde, K. Bajdor, R. Wilbrandt, Through-bond interaction in the radical cation of N,N-dimethylpiperazine. Resonance Raman spectroscopy and quantum chemical calculations. *Chem. Phys. Lett.* **225**, 386–390 (1994).
32. A. M. Brouwer *et al*., Radical cation of N,N-dimethylpiperazine: Dramatic structural effects of orbital interactions through bonds. *J. Am. Chem. Soc.* **120**, 3748–3757 (1998).
33. S. Deb, X. Cheng, P. M. Weber, Structural dynamics and charge transfer in electronically excited N,N′-dimethylpiperazine. *J. Phys. Chem. Lett.* **4**, 2780–2784 (2013).
34. X. Cheng, Y. Zhang, E. Jónsson, H. Jónsson, P. M. Weber, Charge localization in a diamine cation provides a test of energy functionals and self-interaction correction. *Nat. Commun.* **7**, 11013 (2016).
35. Z. A. Ali, F. W. Aquino, B. M. Wong, The diamine cation is not a chemical example where density functional theory fails. *Nat. Commun.* **9**, 4733 (2018).
36. X. Cheng, E. Jónsson, H. Jónsson, P. M. Weber, Reply to: "The diamine cation is not a chemical example where density functional theory fails". *Nat. Commun.* **9**, 5348 (2018).
37. M. Gałyńska, V. Ásgeirsson, H. Jónsson, R. Bjornsson, Localized and delocalized states of a diamine cation: A critical test of wave function methods. arXiv [Preprint] (2020). https://arxiv.org/pdf/2007.06125 (Accessed 15 July 2020).
38. H. T. Philipp, M. Hromalik, M. Tate, L. Koerner, S. M. Gruner, Pixel array detector for X-ray free electron laser experiments. *Nucl. Instrum. Methods Phys. Res. A* **649**, 67–69 (2011).
39. R. C. Dudek, P. M. Weber, Ultrafast diffraction imaging of the electrocyclic ring-opening reaction of 1,3-cyclohexadiene. *J. Phys. Chem. A* **105**, 4167–4171 (2001).
40. B. Stankus *et al*., Advances in ultrafast gas-phase X-ray scattering. *J. Phys. B. Mol. Opt. Phys.* **53**, 234004 (2020).
41. G. Nass Kovacs *et al*., Three-dimensional view of ultrafast dynamics in photoexcited bacteriorhodopsin. *Nat. Commun.* **10**, 3177 (2019).
42. R. J. D. Miller, O. Paré-Labrosse, A. Sarracini, J. E. Besaw, Three-dimensional view of ultrafast dynamics in photoexcited bacteriorhodopsin in the multiphoton regime and biological relevance. *Nat. Commun.* **11**, 1240 (2020).
43. H. Yong *et al*., Determining orientations of optical transition dipole moments using ultrafast x-ray scattering. *J. Phys. Chem. Lett.* **9**, 6556–6562 (2018).
44. J. M. Ruddock *et al*., A deep UV trigger for ground-state ring-opening dynamics of 1,3-cyclohexadiene. *Sci. Adv.* **5**, eaax6625 (2019).
45. E. Prince, *International Tables for Crystallography. Mathematical, Physical and Chemical Tables* (Springer, Dordrecht, ed. 3, 2006).
46. J. P. Dahl, M. Springborg, The Morse oscillator in position space, momentum space, and phase space. *J. Chem. Phys.* **88**, 4535–4547 (1988).
47. H. Yong *et al*., Determination of excited state molecular structures from time-resolved gas-phase X-ray scattering. *Faraday Discuss.*, 10.1039/D0FD00118J (2020).
48. A. Halavanau, F.-J. Decker, C. Emma, J. Sheppard, C. Pellegrini, Very high brightness and power LCLS-II hard X-ray pulses. *J. Synchrotron Radiat.* **26**, 635–646 (2019).
49. A. Moreno Carrascosa, H. Yong, D. L. Crittenden, P. M. Weber, A. Kirrander, Ab initio calculation of total x-ray scattering from molecules. *J. Chem. Theory Comput.* **15**, 2836–2846 (2019).
50. R. M. Parrish, T. J. Martínez, Ab initio computation of rotationally averaged pump probe x-ray and electron diffraction signals. *J. Chem. Theory Comput.* **15**, 1523–1537 (2019).
51. J. G. Kim *et al*., Mapping the emergence of molecular vibrations mediating bond formation. *Nature* **582**, 520–524 (2020).
52. J. M. Budarz *et al*., Observation of femtosecond molecular dynamics via pump-probe gas phase x-ray scattering. *J. Phys. B. Mol. Opt. Phys.* **49**, 034001 (2016).
53. M. R. Bionta *et al*., Spectral encoding method for measuring the relative arrival time between x-ray/optical pulses. *Rev. Sci. Instrum.* **85**, 083116 (2014).
54. J. M. Ruddock *et al*., Simplicity beneath complexity: Counting molecular electrons reveals transients and kinetics of photodissociation reactions. *Angew. Chem. Int. Ed. Engl.* **58**, 6371–6375 (2019).
55. H. J. Werner, P. J. Knowles, G. Knizia, F. R. Manby, M. Schütz, Molpro: A general-purpose quantum chemistry program package. *Wiley Interdiscip. Rev. Comput. Mol. Sci.* **2**, 242–253 (2012).
56. Mai, S. *et al*. SHARC2.1: Surface Hopping Including Arbitrary Couplings – Program Package for Non-Adiabatic Dynamics, sharc-md.org (2019).
57. L. Ma *et al*., Ultrafast x-ray and electron scattering of free molecules: A comparative evaluation. *Struct. Dyn.* **7**, 034102 (2020).
58. H. Gudmundsdóttir, Y. Zhang, P. M. Weber, H. Jónsson, Self-interaction corrected density functional calculations of molecular Rydberg states. *J. Chem. Phys.* **139**, 194102 (2013).
59. J. Enkovaara *et al*., Electronic structure calculations with GPAW: A real-space implementation of the projector augmented-wave method. *J. Phys. Condens. Matter* **22**, 253202 (2010).
60. W. Kohn, L. J. Sham, Self-consistent equations including exchange and correlation effects. *Phys. Rev.* **140**, A1133–A1138 (1965).
61. J. Gavnholt, T. Olsen, M. Engelund, J. Schiotz, Delta self-consistent field method to obtain potential energy surfaces of excited molecules on surfaces. *Phys. Rev. B Condens. Matter Mater. Phys.* **78**, 075441 (2008).